PAPER

An electrochemical immunosensor based on a nano-ceria integrated microfluidic chip for interleukin-8 biomarker detection†

Hema Bhardwaj, Zimad Hashmi, Avinash Kumar Singh, [ID] Gautam Kumar, G. B. V. S. Lakshmi [ID] and Pratima R. Solanki [ID] *

Interleukin-8 (IL8) is an important cytokine that plays a significant role in tumor growth and angiogenesis across various malignant tumors, including oral squamous cell carcinoma (OSCC). It is an important biomarker for oral cancer; therefore, its early and accurate detection in bodily fluid reduces morbidity and mortality rates in cancer patients. The work presents the development of a label-free microfluidic miniaturized electrochemical immunosensor for IL8 biomarker detection at low concentration in saliva samples. A rapid, sensitive and selective biosensing platform was developed for IL8 detection using a nano-ceria integrated microfluidic system. The synthesized nano-ceria particles (8.13 nm) were employed to enhance the electrochemical biosensing signal and sensitivity of the biosensor due to their high catalytic properties and large surface area. For this, microfluidic chip was prepared by Indium tin oxide (ITO) (3 × 4 cm) containing three electrode patterns of working, reference and counter electrode. These electrode patterns were developed using a maskless photolithography technique and a polydimethylsiloxane (PDMS) mold created a 200 μm wide microchannel which was bound to the susbtrate using plasma treatment. Spectroscopy and microscopy techniques were used to confirm the synthesis of nano-ceria. Furthermore, electrode surface modifications were achieved by immobilization of chemically activated antibodies of IL8, as verified by Fourier transform-infrared spectroscopy (FT-IR). Furthermore, differential pulse voltammetry (DPV) was utilized to investigate electrochemical parameters and conduct biosensing studies. The developed electrochemical microfluidic biosensing platform works for an IL8 antigen in the concentrations ranging from 0.004 to 10 ng mL^{-1} with a limit of detection (LOD) and limit of quantification (LOQ) of 0.0001 ng mL^{-1} and 0.0006 ng mL^{-1}, respectively. Moreover, the developed electrochemical biosensing platform was validated using human saliva samples, achieving percentage recovery within an acceptable range.

1. Introduction

With the continuous increase in the number of cancer patients worldwide, early detection of cancer is the most important factor in cancer diagnosis and it has a direct impact on the patient survival rate.[1] Early stage detection of cancer is the most critical step in the successful treatment of cancer.[2,3] This early and accurate detection of cancer can be carried out with certain protein biomarkers present in the blood serum of patients.[1,3] At present, there are various conventional detection techniques available for the detection of these biomarkers, but most of these techniques are expensive and time consuming and require sophisticated equipment with well-trained technical

staff to perform the tests.[3,4] These techniques include enzyme linked immunosorbent assay (ELISA), polymerase chain reaction (PCR), fluorescence assay and mass spectrometric assay.[4–7] But there are certain limitations on their clinical application, such as expensive, the personnel and laborious methods required, the low sensitivity and high detection limit attained, and they are time consuming. These limitations suggest a pathway for the development of biosensors for cancer biomarker detection which are capable of showing a selective and sensitive immunological response.[7,8] This is beneficial as it reduces the cost of diagnosis and helps in fundamental understanding of cancer at an early stage.[9] In this context, extensive research has been carried out in recent years on point-of-care (POC) devices for the detection of oral cancer biomarkers.[8] Researchers in these fields tend to develop biosensing devices which combine an antibody as a recognition element with a transducer that converts an electrical signal into a measurable signal generated due to the interaction between the antigen and the antibody.[10,11]

Nano-Bio Laboratory, Special Centre for Nanoscience (SCNS), Jawaharlal Nehru University, New Delhi 110067, India. E-mail: partima@mail.jnu.ac.in; pratimarsolanki@gmail.com

† Electronic supplementary information (ESI) available. See DOI: https://doi.org/10.1039/d4na00636d

Oral cancer has been a major cause of concern over the last century as cases have seen an increasing trend over each decade. According to data given by the International Agency of Research on Cancer, there were more than 0.3 million new cases of lip and oral cavity cancer reported all over the world. In 2020, there were more than 0.1 million deaths reported worldwide due to oral cancer. Even in India, oral cancer is the most common cancer among men and the third most common cancer among women. According to earlier reported data, out of every 0.1 million population twenty people have been reported to be suffering from oral cancer.[12]

IL8 is a well-known protein manufactured by the immune system of the human body. It is categorized as an 8 kDa cytokine that causes inflammation in a cancer patient with serum levels of 20–1000 pg mL^{-1} (0.02–1 ng mL^{-1}) in comparison with serum levels of <13 pg mL^{-1} in a healthy person.[13] IL8 cytokine is essential for both diagnosis and treatment since concentration has been found to increase in various types of cancers, including squamous cell cancer,[14] prostate cell carcinoma,[15] thyroid cancers,[15] and pancreatic cancer.[15]

In recent research, IL8 has been reported as an important biomarker for the diagnosis of oral malignancy, OSCC.[16,17] IL8 cytokines are a kind of intercellular signaling protein categorized as non-structural proteins.[18] Recent studies on cytokines revealed that the pro-inflammatory activity of IL8 shows diagnostic potential for detection of early stage oral cancer.[19] It has been reported that in OSCC patients, there is a significant elevation in the values of IL8 cytokine, which can easily be identified by a diagnostic technique.[20]

A biosensor is an advanced analytical device for the early, sensitive, selective and specific detection of an analyte in a short period of time.[21] The electrochemical biosensing performance of a device, such as sensitivity, specificity, and stability of the sensor, are certainly enhanced by the use of nanomaterials, including graphene oxide, carbon nanotubes, and metal oxide nanoparticles.[22] Among these various materials, cerium oxide (Ceria, CeO$_2$) is a well-known rare earth metal oxide due to its intriguing physical, chemical and mechanical properties. Nano-ceria shows tremendous properties owing to its unique characteristics, such as high mechanical strength, oxygen ion conductivity, wide band gap (3.4 eV), biocompatibility, low cost, good stability, strong biological activities and many other advantages.[23] Nano-ceria possesses good electrochemical catalytic properties and acts as a biological antioxidant due to the Ce^{3+}/Ce^{4+} charged moieties on the nano-ceria particles which making them an excellent candidate for biosensing applications.[23] Thus, integration of nano-ceria onto an electrode surface not only functionalizes the electrode surface and provides biocompatibility but also amplifies the electrochemical signals. This enhancement in signal response improves stability and sensitivity of the biosensor owing to the higher surface area and the abundance of active sites that facilitate better adsorption of biomolecules. The chemically activated biomolecules *via* N-ethyl-N-(3-dimethylaminopropyl)-carbodiimide (EDC) and N-hydroxysuccinimide (NHS) chemistry, bind to the available oxygen group moieties of nano-ceria resulting in significant enhanced binding with IL8 and

improved overall electrochemical biosensing signals. A few reports have been published related to the use of nano-ceria to achieve better electrochemical biosensing performance for the construction of biosensors for the detecting various analytes such as toxins or dopamine.[24] For example, Dhiman *et al.* demonstrated the detection of mycotoxin ochratoxin-A using cerium oxide nanoparticles. They found good electrochemical biosensing performance with improved sensitivity, selectivity, and low LOD over a wide detection range.[25] Similarly, Gomes-Junior *et al.* developed an electrochemical sensor for dopamine detection in biological fluid using ultrasmall cerium oxide nanoparticles.[24] The sensor showed excellent electrochemical performance in terms of stability and repeatability, with an adequate detection limit for dopamine in urine samples. These studies indicate that nano-ceria is a highly effective material for constructing sensitive and selective biosensors for various analyte detection.

For the onsite and portable detection of an analyte using a biosensing platform, the effect of an open environment on sensing results reduced biosensor performance. Recently, researchers have focused on miniaturization of a POC device that can be easy to use, portable, with a low sample volume requirement, ultraprecise and clinically applicable.[26] Therefore, a microfluidic-based bioanalytical detecting device is a highly advanced platform that provides a compact and portable single chip unit system with 10–200 μm of microchannels that allow a small amount of fluid to flow in a laminar motion.[27] Therefore, a microfluidic system used for the construction of a biosensor provides a miniaturized closed and stable environment with a reduced sensing area, resulting in enhanced sensitivity and reliability for the device. Microfluidic-based devices offer several advantages compared to conventional techniques, such as throughput processing, low sample volume requirement, enhanced transport for controlling the flow conditions, real-time monitoring, a simplified testing process, a portable device, cost-effectiveness and a faster response time.[28,29] The small dimensions of a microfluidic chip provide a high surface-to-volume ratio, surface tension, laminar flow and capillary effect, which expand their use for portability and on-site testing.[30] Many scientific researchers have focused on the development of early and accurate detection of the IL8 biomarker for oral cancer. For example, Verma *et al.* developed a gold nanoparticles-reduced graphene oxide (AuNPs–rGO) based immunosensor for non-invasive electrochemical detection of IL8 in saliva samples.[31] This biosensor showed a linear current response with increasing concentrations of IL8 from 0.0005 to 4 ng mL^{-1} with LOD of 0.072 ng mL^{-1}. Moreover, the developed immunosensor was tested in human saliva samples and showed an average percentage recovery of 94.15%. Other work published by Pachauri *et al.* related to the construction of a silver molybdate nanomaterial based electrochemical immunosensor for IL8 biomarker detection. The developed immunoelectrode exhibited improved biosensing characteristics with a linear detection response ranging from 1 fg mL^{-1} to 40 ng mL^{-1} with LOD of 0.09 ng mL^{-1}.[32] Although numerous research articles have been explored for the development of a biosensor for IL8 detection, to the best of our knowledge, no studies have been reported using

a microfluidic-based electrochemical biosensor for detecting IL8 in human saliva samples. Although a few studies have been reported for the detection of single or multiple biomarkers, including IL8, using a microfluidic processing unit by an optical/fluorescence spectroscopy technique.[33,34] Therefore, to the best of our knowledge this is the first time a microfluidic electrochemical biosensing device has been reported for non-invasive IL8 biomarker detection in human saliva samples.

In this context, a nano-ceria based microfluidic integrated electrochemical biosensor was fabricated for the early stage detection of IL8 biomarker in saliva samples. A simple and effective co-precipitation method was used for the synthesis of nano-ceria. For the design and preparation of a microfluidic chip, a maskless photolithography system was used to develop three electrodes on an ITO-covered glass electrode comprised of working, reference and counter electrodes bound by a PDMS soft elastomer with a 200 μm micro-channel. The developed microfluidic nano–biochip of BSA/anti-IL8/nano-ceria/ITO was utilized for IL8 biomarker detection. The electrochemical response signals of the fabricated immunoelectrode BSA/anti-IL8/nano-ceria/ITO towards various concentrations of IL8 biomarker were achieved using DPV technique. The developed nano-ceria based microfluidic system was tested in human saliva samples and an interference study was performed to obtain the specificity and selectivity of the developed biosensor towards the IL8 biomarker.

2. Experimental section

2.1 Chemicals and reagents

Monoclonal antibodies of IL8 (anti-IL8), the antigen of IL8, were procured from Abcam Company, UK. Cerium(III) nitrate hexahydrate, sodium hydroxide, sodium phosphate monobasic anhydrous (NaH_2PO_4) and sodium phosphate dibasic dehydrate (Na_2HPO_4), N-ethyl-N-(3-dimethylamino propyl)carbodiimide (EDC), N-hydroxysuccinimide (NHS), sodium chloride, potassium chloride, and Bovine Serum Albumin (BSA) were purchased from SRL, India. Cancer antigen (CA)-125 was purchased from MedChemExpress, India. Nitric acid (HNO_3), hydrochloric acid (HCl), Cyfra-21, tumor necrosis factor (TNF-α), and carcinoembryonic antigen (CEA) were purchased from MedChemExpress, India. Potassium ferricyanide [$K_3[Fe(CN)_6]$] and potassium ferrocyanide [$K_4[Fe(CN)_6]$] were purchased from Fisher Scientific. SYLGARD 184 PDMS silicon elastomer and curing agent were purchased from Merck, India. ITO-covered glass substrate was purchased from Blazers, UK. Millipore-purified deionized water of 18.2 MΩ cm resistivity was used for the buffer and the preparation of all other solutions. 0.2 M of phosphate buffered solution (PBS) was prepared with 0.9% NaCl and 5 mM of electrolyte [$Fe(CN)_6]^{3-/4-}$ with pH 7.4. SU8 and AZ1512 photoresist were bought from Kayaku Advanced Materials and AZ Electronic Materials. An aqueous solution of IL8 was prepared in 0.2 M PBS (pH 7.4).

2.2 Instruments

Structural, optical and electrochemical properties of the synthesized nano-ceria and fabricated microfluidic chip were investigated using spectroscopic, microscopic and electrochemical techniques. UV-visible absorbance studies were carried out using a UV-2450 UV-visible spectrophotometer. XRD patterns and planes were examined with a Rigaku MiniFlex 600 X-ray diffractometer with Cu Kα radiation ($\lambda = 1.54$ Å) within the 2θ range of 10–80°. FT-IR studies were carried out to determine the presence of functional groups, bonding and stretching vibrations using a PerkinElmer UATR Spectrum – Two FT-IR spectrophotometer at a resolution of 4 cm^{-1}. Raman spectroscopy measurements were performed using an EnSpectra R532 laser from WITEC, USA. The surface morphology of nano-ceria was explored with a field emission scanning electron microscope (FESEM, Zeiss Gemini SEM 500 thermal field emission type) equipped with an energy dispersive X-ray detector (EDX). Structural investigation was done using high resolution HR-TEM with a JEOL JEM-2200 FS, Japan. All cyclic voltammetry (CV), DPV, and electrochemical impedance spectroscopy (EIS) electrochemical measurements were conducted using a Metrohm Autolab (AUT86014) instrument.

2.3 Synthesis of nano-ceria

Nano-ceria was prepared using a previously reported co-precipitation method with slight modifications.[35] In detail, 0.25 M of cerium nitrate was taken in a 250 mL beaker and dissolved in distilled water. After that, 0.1 M of sodium hydroxide solution was added drop by drop until the pH reached 12 and a yellow-coloured precipitate formed. The precipitate was filtered out using Whatman filter paper and dried overnight in an oven at 80 °C. Then the dried powder was calcined at 350 °C for 2 hours and yellow-coloured nano-ceria powder was obtained.

2.4 Preparation of microfluidic chip by maskless lithography

A PDMS channel of 200 μm was fabricated using a soft photolithography technique. The negative photoresist SU-8 chemical was used for spin coating onto a silicon wafer. Then wafer was heated at 100 °C to evaporate solvent present over silicon surface and kept for exposure under UV radiation through a desired mask. It was heated again and unexposed SU-8 was removed with SU-8 developer.[36] The silicon elastomer and curing agent were mixed in 10 : 1 ratio (v/v) to make a PDMS mixture. This mixture was poured onto a silicon wafer, and kept in the oven at 80 °C for 120 minutes to obtain the PDMS matrix. The PDMS replica with a channel height of 2 cm and width of 200 μm was carefully peeled off.[36] Scheme 1 presents the step-wise preparation of microfluidic chip using the maskless lithography technique.

For the fabrication of microelectrodes onto an ITO-coated glass substrate (3 × 4 cm), a positive (AZ1512) photoresist was coated using a spin coater at 1500 rpm at room temperature to obtain a uniform photoresist film. Then a pre-baking process was performed by keeping the coated ITO on a hot plate at 80 °C to remove moisture from the surface and placed into the photolithography instrument. Clewin software was used to design a three-electrode pattern. This designed pattern was transferred onto photoresist ITO-coated film using
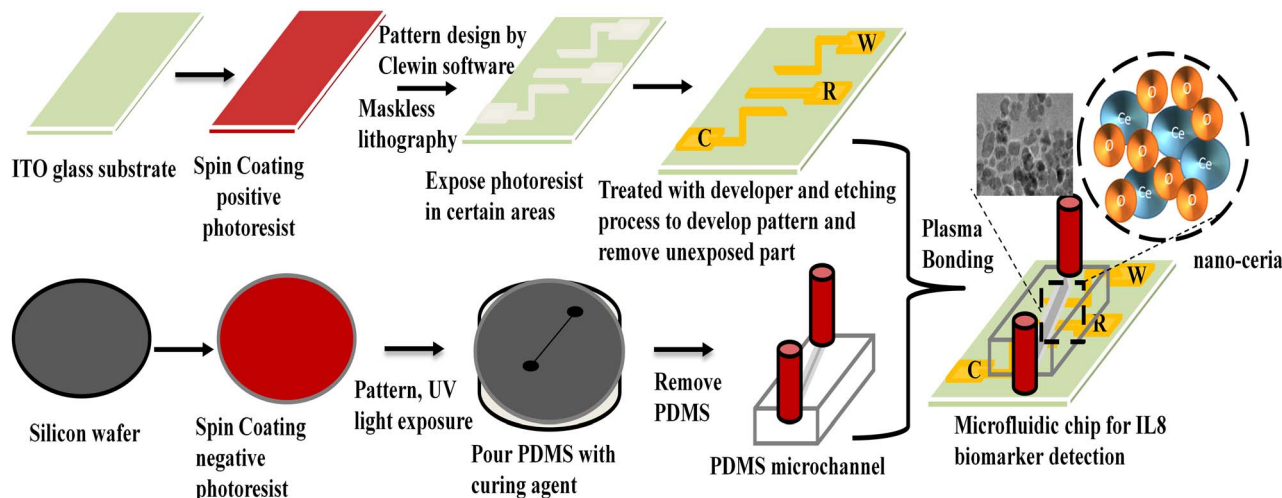
Scheme 1 Steps for the preparation of a microfluidic chip using the maskless lithography technique.

a photolithography technique through UV exposure. After that, the exposed film substrate was kept at 80 °C for 10 minutes for the post-baking process and transferred into an AZ photoresist developer solution to remove the unexposed area. The prepared glass substrate containing the developed patterns of the three electrodes was dipped into an etching solution mixture of HNO_3, HCl, and H_2O for 5 minutes to remove the ITO conducting part except for the ITO patterned area. Isopropanol solvent was used to clean the surface of microelectrode chip. After that, a hydrolysis process was carried out using a solution mixture containing 1 : 1 : 5 v/v/v of NH_3 : H_2O_2 : H_2O and kept in the oven at 80 °C for 30 minutes, afterthat washed with distilled water.[37]

2.5 Fabrication of BSA/anti-IL8/nano-ceria/ITO microfluidic nano–biochip

A 1 mg per mL concentration of synthesized nano-ceria was prepared in distilled water and sonicated for 30 minutes then drop-casted onto working area of electrode. The prepared electrodes were left to dry overnight at room temperature. Silver paste (Ag/AgCl) was used as reference electrode. After that, prepared microelectrode chip and PDMS matrix were bonded with Novascan plasma binder. For immobilization of the antibodies onto nano-ceria/ITO substrate, anti-IL8 (5 μg mL^{-1}) was mixed with EDC : NHS solution, and kept at 4 °C for 30 minutes for activation of –COOH groups of anti-IL8. Activated anti-IL8 antibodies were uniformly spread over nano-ceria/ITO surface and kept in a humid chamber for 4 hours. 10 μL of BSA was drop-casted anti-IL8/nano-ceria/ITO to block non-specific active binding sites, further washed with PBS.[38] The fabricated BSA/anti-IL8/nano-ceria/ITO nano–biochip was kept at 4 °C until further use.

2.6 Preparation of spiked IL8 samples

Fresh saliva samples were used for the real sample application of a BSA/anti-IL8/nano-ceria/ITO nano–biochip. Saliva spiked samples were prepared by adding 5 μL of saliva and 5 μL of

standard antigen of IL8 concentrations of 0.1, 0.4 and 2 ng mL^{-1}. DPV studies were performed to measure the current response with each spiked concentration of IL8. To carry out this study, the flow rate of the fluid was maintained at 20 μL min^{-1}. The ethical committee of the All India Institute of Medical Sciences (AIIMS) and Jawaharlal Nehru University (JNU) New Delhi, India provided ethical clearance.

3. Results and discussion

3.1 Optical and morphological characterization

Fig. 1 shows a schematic description of the synthesis of nano-ceria using a co-precipitation method followed by the calcination process and fabrication of microfluidic nano–biochip for IL8 biomarker detection using an electrochemical DPV technique.

Preliminary confirmation of the absorption peak and energy band gap of nano-ceria was investigated by UV-visible spectroscopy. Fig. 2 shows the UV-visible spectrum of nano-ceria. The absorption peak appearing at 268 nm is mainly caused by the charge transfer transition taking place from $O^{2-}(2p)$ to the $Ce^{4+}(4f)$ orbital in CeO_2 states.[30] The indirect band gap of nano-ceria was calculated using eqn (1):[39]

$$\alpha = \frac{A\left(h\nu - E_g\right)^{1/2}}{h\nu} \tag{1}$$

where α is the optical absorption coefficient, $h\nu$ is the energy of a photon, E_g is the energy of the band gap, A is a constant that depends on the transition probability. The inset image in Fig. 2 presents the Tauc plot of nano-ceria and the measured energy band gap was found to be 4.07 eV.

The diffraction pattern of nano-ceria was examined by XRD. Fig. S1a(ii)† presents the XRD spectrum of nano-ceria, where a sharp intense peak appeared at 28.2° corresponding to (111) planes. Other peaks appeared at 33°, 47.44°, 56.12°, 69.3° and 76° corresponding to (200), (220), (311), (400), and (331) planes, respectively.[30] These peaks are indexed as a face centered lattice cubic fluorite structure with the *Fm*3*m* (225) space group of
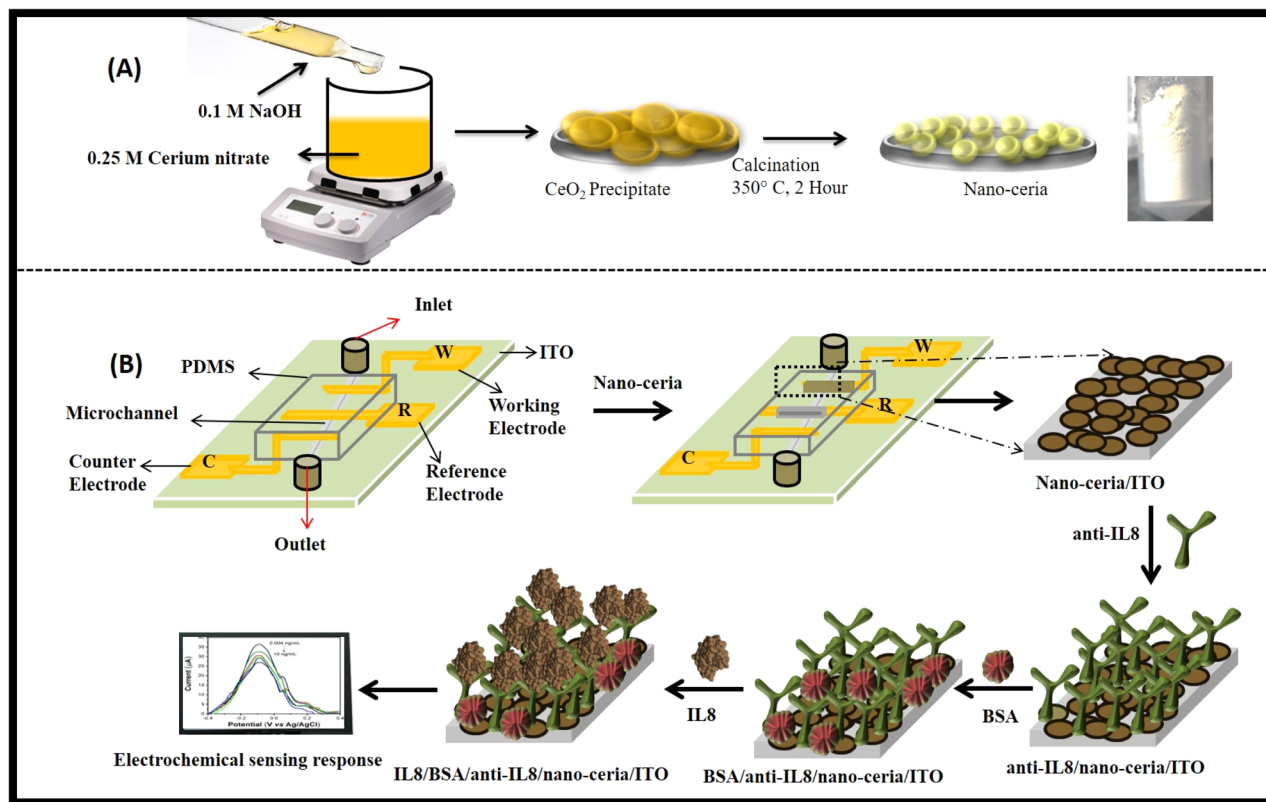
Fig. 1 Schematic illustration of (A) the synthesis of nano-ceria using co-precipitation method and (B) the fabrication of a nano−biochip for the development of a microfluidic device for IL8 biomarker detection by DPV technique.
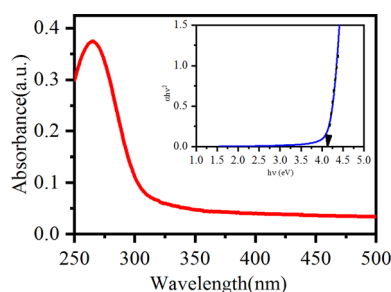

Fig. 2 UV-visible spectrum of synthesized nano-ceria (inset: Tauc plot of nano-ceria).

nano-ceria, matching the reference standard peak of CeO_2 shown in Fig. S1a(i)† [JCPDS file no. 81-0792]. Also, the average crystallite size of synthesized nano-ceria was evaluated using the Scherrer eqn (2):[39]

$$D = \frac{0.9\lambda}{\beta \cos \theta} \quad (2)$$

where D is the average crystallite size, λ is the X-ray source wavelength (0.154 nm) for Cu Kα radiation, β is the full width half maximum (FWHM), and θ is the diffraction angle. The average calculated crystallite size of nano-ceria was 7 nm.

Fig. S1b† displays the Raman spectrum of synthesized nano-ceria, where the intense peak appearing at 464 cm^{-1} corresponds to the triply degenerate Raman active mode due to the

cubic structure of nano-ceria. The other peaks appearing at 117 cm^{-1} was ascribed to transverse optical doubly degeneracy and at 607 cm^{-1} is due to the longitudinal mode of the oxygen vacancy and intrinsic defects.[39] A small peak was also observed at 1050 cm^{-1} attributed to isolated surface defect sites.

The existence of functional groups and the attachment of the nano-ceria with antibodies was confirmed by FT-IR spectroscopy. Fig. S2† illustrates the FT-IR spectrum of (i) synthesized nano-ceria and (ii) antibodies immobilized on nano-ceria. In Fig. S2(i),† the peaks appearing at 3386 and 1034 cm^{-1} are due to –OH stretching and bending vibrations. The other peaks appearing at 2986 and 2886 cm^{-1} correspond to asymmetric and symmetric –CH stretching vibrations. The peaks appearing at 1620 and 1348 cm^{-1} result from O–C–O bonds. The sharp peak appearing at 486 cm^{-1} is attributed to Ce–O bonding. Additionally, apart from the appearance of the FT-IR peaks shown in Fig. S2(i),† some other peaks also appearing in the spectrum of Fig. S2(ii)† at 3400 and 1735 cm^{-1} are attributed to primary and secondary amide bonding, respectively.[40] These results confirm the bonding of immobilized antibodies of IL8 with nano-ceria.

TEM images of the synthesized nano-ceria are presented in Fig. 3(a)–(d). Fig. 3(a)–(c) display TEM micrographs of synthesized nano-ceria *via* co-precipitation method. The obtained nano-ceria is spherical and homogeneous as well as being monodispersed with an approximate diameter of 8.13 nm (inset image of Fig. 3(a)). These spherical nanoparticles were also
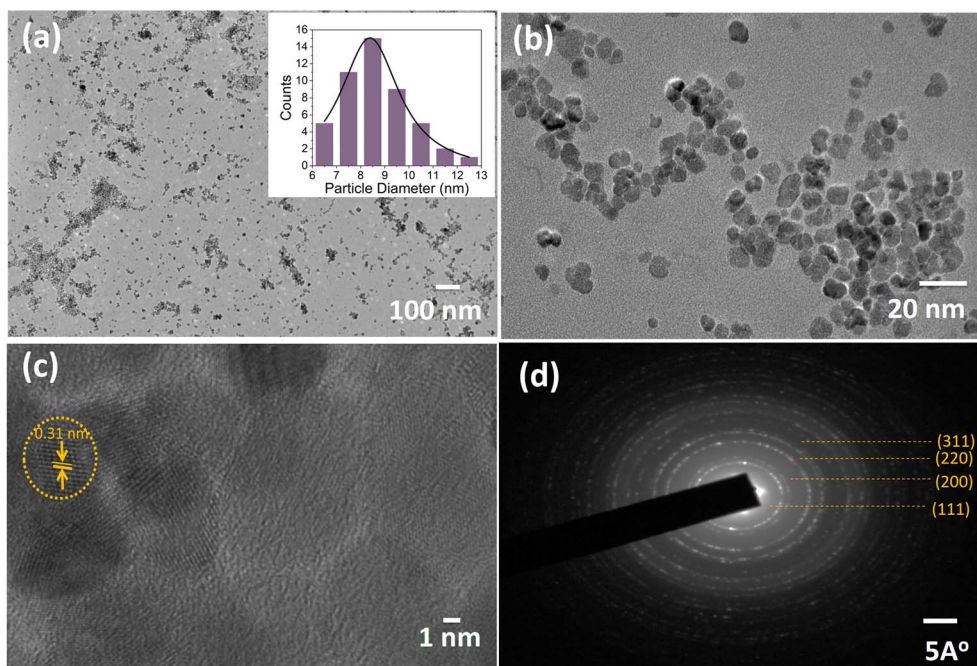
Fig. 3 TEM images of synthesized nano-ceria (a–c) [inset: (a) histogram of particle size distribution] and (d) SAED pattern of nano-ceria.

confirmed by HR-TEM (Fig. 3(c)) and show distinct fringes with a *d*-spacing of 0.31 nm attributed to the (111) plane. Also, the selected area electron diffraction (SAED) pattern of nano-ceria is depicted in Fig. 3(d). The fine rings indexed to (111), (200), (220), and (311) are in agreement with the fluorite cubic structure and high crystallinity of nano-ceria.

FE-SEM and EDX studies of nano-ceria were carried out for surface morphology and elemental composition analysis and the obtained images are shown in Fig. S3a–f.† The appearance of small nano-ceria with uniform spherical morphology, as shown in Fig. S3a and b,† is consistent with the TEM results. Additionally, the elemental composition in nano-ceria was also investigated by EDX and the obtained spectrum is shown in Fig. S3c.† The presence of cerium and oxygen elements in the composite of nano-ceria confirms the formation of nano-ceria with highest purity. Moreover, elemental mapping studies were carried out and the images are shown in Fig. S3d–f.† Fig. S3d† presents the SEM elemental mapping of the materials and the obtained results confirm the presence of cerium and oxygen elements in the composition of the materials. Also, separate images were taken, as shown in Fig. S3e and f,† defined by the presence of individual distinguishing colors, prove the existence of both cerium and oxygen elements alone.

3.2 Electrochemical studies of modified multilayered surfaces

CV measurements were accomplished to explore the electrochemical behavior and interfacing activity of nano-ceria/ITO, anti-IL8/nano-ceria/ITO and BSA/anti-IL8/nano-ceria/ITO in 0.2 M PBS with a 5 mM ferri–ferro redox mediator at a 50 mV s^{-1} scan rate. Also, electrochemical parameters such as diffusion coefficient, surface concentration, and anodic and cathodic

peak current values were determined using CV studies. The CV measurements results of various modified electrode surfaces are depicted in Fig. 4(a). The anodic and cathodic peak current values for the nano-ceria/ITO electrode surface were measured at 463 µA and −416 µA, respectively, showing a higher current response compared to other modified electrode surfaces (such as with antibodies or BSA). The high electrochemical current value observed at the nano-ceria electrode surface can be attributed to its large surface area and better superficial heterogeneous electron transfer (HET) properties, which provide remarkable electron conductivity. Then, anti-IL8 antibodies were immobilized onto the nano-ceria surface and the corresponding CV was taken. The anodic and cathodic peak current values decreased to 357 µA and −324 µA, respectively. This reduction is attributed to the presence of antibodies, which creates an obstacle in processing of electron transfer between the electrode and redox couple electrolyte. Subsequently, after treatment with BSA protein on the anti-IL8/nano-ceria/ITO electrode surface, which helps to block the present non-specific sites on the surface, the current responses decreased significantly to 306 µA and −265 µA for the anodic and cathodic peak currents, respectively. This decrease in the peak current values reveals that transportation of electrons between the electrode and electrolytic redox medium is hindered by the presence of the bulky biomolecular structure protein on the anti-IL8/nano-ceria/ITO surface.

Moreover, the electrochemical behavior of the modified electrode surfaces, such as nano-ceria/ITO, anti-IL8/nano-ceria/ITO and BSA/anti-IL8/nano-ceria/ITO, were also studied by EIS. EIS is a label-free technique used to determine the charge transfer process and adsorption behavior of biomolecules in a redox electrolyte species. EIS measures the AC impedance
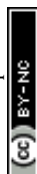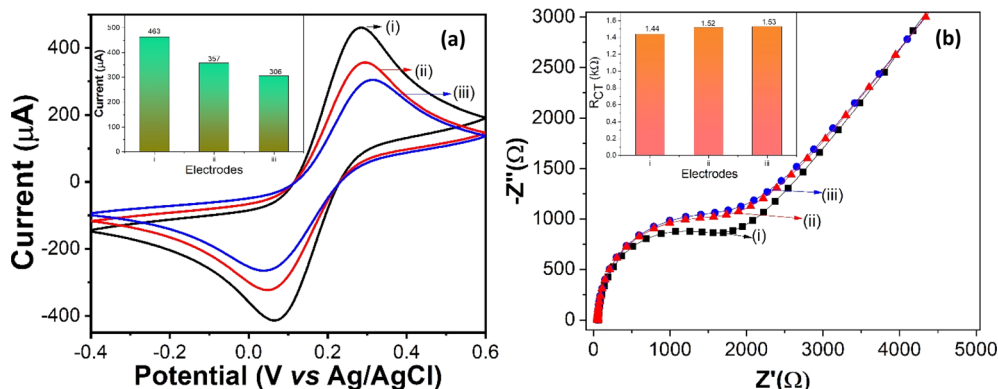
Fig. 4 (a) Cyclic voltammetry studies of (i) nano-ceria/ITO, (ii) anti-IL8/nano-ceria/ITO, (iii) BSA/anti-IL8/nano-ceria/ITO electrodes (b) electrochemical impedance response signal of (i) nano-ceria/ITO, (ii) anti-IL8/nano-ceria/ITO, (iii) BSA/anti-IL8/nano-ceria/ITO electrodes conducted in PBS (pH 7.4) containing $[Fe(CN)_6]^{3-/4-}$.

signal in the frequency range of 0.1 to 10^4 Hz. The resulting Nyquist plot displays a semicircle diameter, indicating that charge transfer resistance (R_{CT}) occurs in the higher frequency region while mass transfer process are observed at low frequencies. For analysis of EIS Nyquist plot data, the Randles equivalent circuit is used, which is composed of solution resistance (R_s) in series with a parallel combination of double-layer capacitance (C_{dl}), R_{CT} and Warburg impedance (Z_W). Electrochemical measurements of modified electrodes were conducted using an EIS analyzer in 0.2 M PBS containing 5 mM ferri–ferro redox mediator. Fig. 4(b) shows the electrochemical impedance behavior of nano-ceria/ITO, anti-IL8/nano-ceria/ITO and BSA/anti-IL8/nano-ceria/ITO electrodes. The R_{CT} value for the nano-ceria/ITO electrode was found to be 1.44 kΩ, for anti-IL8/nano-ceria/ITO it was 1.52 kΩ and for BSA/anti-IL8/nano-ceria/ITO it was 1.53 kΩ. It is important to note that the lower R_{CT} value found for the nano-ceria electrode surface is primarily due to its conductivity and shortening of the electron diffusion path, which enhance the charge transfer electron process. After the immobilization of the anti-IL8 onto the nano-ceria electrode surface, the R_{CT} value increases to 1.52 kΩ, mainly due to the immobilization of macromolecules (anti-IL8) conjugated over the nano-ceria that hinders charge transfer between the electrode and electrolyte. Further, for anti-IL8/nano-ceria/ITO treated with BSA, the R_{CT} value increased to 1.53 kΩ due to the presence of BSA, which blocks non-specific active sites on the anti-IL8/nano-ceria/ITO surface.

The value of the important parameter heterogeneous electron transfer (HET) was calculated for the modified electrodes to determine the electrochemical characteristics, specifically the electron transfer rate.

The HET values of fabricated electrodes with nano-ceria/ITO, anti-IL8/nano-ceria/ITO and BSA/anti-IL8/nano-ceria/ITO were calculated using eqn (3):[37]

$$K_e = \frac{RT}{n^2 F^2 A R_{CT} S} \qquad (3)$$

where R represents the gas constant (8.314 J K^{-1} mol^{-1}), T is temperature (298 K), n is the number of electrons transferred *i.e.*

1, F is the Faraday constant (96 500 C mol^{-1}), A is the effective area of the electrode, R_{CT} is the charger transfer resistance value (Ω), and C is the concentration of the redox probe. The HET value for the nano-ceria/ITO surface was found to be 7.390×10^{-6} cm s^{-1} and for anti-IL8/nano-ceria/ITO and BSA/anti-IL8/nano-ceria/ITO the HET values were found to be 7.001×10^{-6} cm s^{-1} and 6.95×10^{-6} cm s^{-1}. The higher HET value for nano-ceria/ITO is due to the electrochemical conductivity that provides the easiest path for the transfer of electrons. However, after the immobilization of anti-IL8, the HET value increased due to the large antibody group present on the surface, which restricts the transfer of electrons between the electrode and the electrolyte medium.

3.3 Optimization studies

Optimization of antibody concentration is a very important step for the construction of an electrochemical biosensor in order to get the best sensor performance. Therefore, in this present work, concentration optimization of antibodies was carried out using cyclic voltammetry. In order to determine the optimum amount of anti-IL8 required on the nano-ceria/ITO substrate, different concentrations of antibodies were immobilized to measure the loading capacity of the fabricated electrode. Fig. S4a† shows the current signal response with various concentrations of anti-IL8 ranging from 0 to 20 μg mL^{-1}. It clearly indicates that after the immobilization of antibodies onto the nano-ceria electrode surface, the current signal decreases due to the loading of macromolecular (anti-IL8) biomolecules that hinder the transfer of electrons between electrode and electrolyte. Further, by increasing the anti-IL8 concentration from 10 to 20 μg mL^{-1}, almost the same current response was obtained due to saturation over the electrode surface. Therefore, a 5 μg mL^{-1} concentration of anti-IL8 was selected for the fabrication of an electrochemical immunosensor for IL8 detection.

A pH optimization study was also carried out to identify the most suitable pH of PBS buffer for the electrochemical sensor performance of the BSA/anti-IL8/nano-ceria/ITO immunoelectrode. For this study, PBS buffers of various pH containing redox

species were prepared, *i.e.* in the range of 6.0 to 8.0, and the electrochemical response was assessed using CV at a 50 mV s^{-1} scan rate. Fig. S4b† shows the variation in current signal responses attained with respect to the change in the pH of the PBS buffer. In this regard, the electrode fabricated with BSA/anti-IL8/nano-ceria/ITO shows a maximum current value with PBS buffer of pH 7.4; therefore, the results imply that the antibody exhibits great stability and activity at pH 7.4. Therefore, pH 7.4 is most suitable for an antibody to maintain its morphological characteristics and to minimize denaturing of the antibody under acidic or basic conditions (H$^+$ or OH$^-$ ions).

Fig. S5a and c† illustrates the CV scan rate studies of nano-ceria/ITO and BSA/anti-IL8/nano-ceria/ITO electrodes in the scan rate range from 10 to 100 mV s^{-1}. Fig. S5a and c† show that anodic and cathodic peak current values increased with increasing scan rate from 10 to 100 mV s^{-1}. The obtained curves reveal that the process is diffusion controlled, demonstrating facile electron transfer between the electrode surface and the electrolyte redox medium. As the scan rate increased, the size of the diffusion layer decreased. Fig. S5b and d† display that the current response signals of the anodic and cathodic peaks current increase linearly with the square root of scan rate and linear response eqn (4)–(7) are as follows:

$$I_a = 28.31\ \mu A + 45.48\ \mu A\ [mV\ s^{-1}]^{-1/2} \times scan\ rate\ [mV\ s^{-1}]^{-1/2},$$
$$R^2 = 0.9986 \tag{4}$$

$$I_c = -56.64\ \mu A - 36.45\ \mu A\ [mV\ s^{-1}]^{-1/2} \times scan\ rate\ [mV\ s^{-1}]^{-1/2},$$
$$R^2 = 0.9964 \tag{5}$$

$$I_a = 25.84\ \mu A + 39.92\ \mu A\ [mV\ s^{-1}]^{-1/2} \times scan\ rate\ [mV\ s^{-1}]^{-1/2},$$
$$R^2 = 0.9931 \tag{6}$$

$$I_c = -48.83\ \mu A - 31.36\ \mu A\ [mV\ s^{-1}]^{-1/2} \times scan\ rate\ [mV\ s^{-1}]^{-1/2},$$
$$R^2 = 0.9999 \tag{7}$$

where I_a is the anodic peak current, I_c is the cathodic peak current, and R^2 is the regression coefficient.

Using the Randles–Ševčík equation, the diffusion coefficient at electrode surface with the redox probe was calculated using eqn (8):[41]

$$I_p = 2.69 \times 10^5 n^{3/2} A D^{1/2} V^{1/2} C \tag{8}$$

where I_p is the peak current value of the electrode surface (A), n is the number of electrons involved in the reaction ($n = 1$), C is the concentration of redox species (5 mM), A is the effective surface area of the electrode, D represents the diffusion coefficient, and V is the scan rate (50 mV s^{-1}). The calculated diffusion coefficient value for the nano-ceria/ITO electrode was found to be 9.5×10^{-6} cm^2 s^{-1}, for the anti-IL8/nano-ceria/ITO electrode it was 5.65×10^{-6} cm^2 s^{-1} and for the BSA/anti-IL8/nano-ceria/ITO electrode it was 4.1×10^{-6} cm^2 s^{-1}. The high value for the diffusion coefficient of the nano-ceria electrode is attributed to high ionic conductivity and provides easiest path to transfer the electron between the electrode and electrolyte interface during electrolytic reactions.

Moreover, the surface concentration of ionic electroactive species was calculated using the Brown–Anson eqn (9):[42]

$$I^* = \frac{4RTI}{n^2 F^2 A\nu} \tag{9}$$

where R is the gas constant (8.314 mol^{-1} K^{-1}), T is room temperature (300 K), F is the Faraday constant (96 485 C mol^{-1}), I is the anodic peak current value of the electrode, and ν is the scan rate (0.05 V s^{-1}). For the nano-ceria/ITO electrode, the surface concentration was found to be 1.97×10^{-8} mol cm^{-2} and for the anti-IL8/nano-ceria/ITO and BSA/anti-IL8/nano-ceria/ITO surfaces, the surface concentration decreased to 1.47×10^{-8} mol cm^{-2} and 1.30×10^{-8} mol cm^{-2}, respectively. The high value of surface concentration for nano-ceria is attributed to the large surface-to-volume ratio and high electrochemical conductivity. However, the surface ionic conductivity decreased with surface modification by immobilization of antibodies of IL8 and BSA. These results are attributed to the existence of heavy molecules over the electrode surface that hindered electron transportation through the redox couple of ferri–ferrocyanide in the electrolyte solution, resulting in a decrease in surface concentration.

Analysis of the behavior of surface-modified electrodes of nano-ceria/ITO, anti-IL8/nano-ceria/ITO and BSA/anti-IL8/nano-ceria/ITO determined by CV or EIS was used to obtain electrochemical properties such as diffusion coefficient, surface concentration, oxidation and reduction peak currents, impedance response, and scan rate studies. Microfluidic chips prepared with nano-ceria/ITO, anti-IL8/nano-ceria/ITO and BSA/anti-IL8/nano-ceria/ITO were used to study further electrochemical signal and biosensing responses for IL8 biomarker detection.

Electrochemical characterization studies of nano-ceria/ITO, anti-IL8/nano-ceria/ITO and BSA/anti-IL8/nano-ceria/ITO surfaces were examined through DPV. Fig. 5(a) illustrates the DPV response of (a) nano-ceria/ITO, (b) anti-IL8/nano-ceria/ITO, and (c) BSA/anti-IL8/nano-ceria/ITO electrodes inside a microfluidic chip with a flow rate of 20 μL min^{-1}. The magnitudes of the peak current values of (a) nano-ceria/ITO, (b) anti-IL8/nano-ceria/ITO, and (c) BSA/anti-IL8/nano-ceria/ITO electrodes changed, confirming stepwise surface modification of the microfluidic chip. The highest current value (46.16 μA) obtained for nano-ceria on the ITO substrate, ascribed to the large surface-to-volume ratio, tremendous adhesion, good permeability and great electro-catalytic activity. Thereby, nano-ceria provides sufficient electron conductivity and also promotes electron transfer between electrode–electrolyte surfaces. Therefore, the presence of nano-ceria over the ITO electrode surface provides a favorable environment for immobilization of antibodies of anti-IL8. The EDC : NHS functionalized antibodies of anti-IL8 provide an activated –COOH group to positively charge the surface of nano-ceria, and the Y-shaped molecule of the antibodies containing two arms and a stem connected by disulfide linkage allows flexible movement into the antibody to bind with the nanoparticle surface. The activated anti-IL8 has affinity for binding with positively charged nano-ceria and can also bind with available oxygen groups of the moieties.
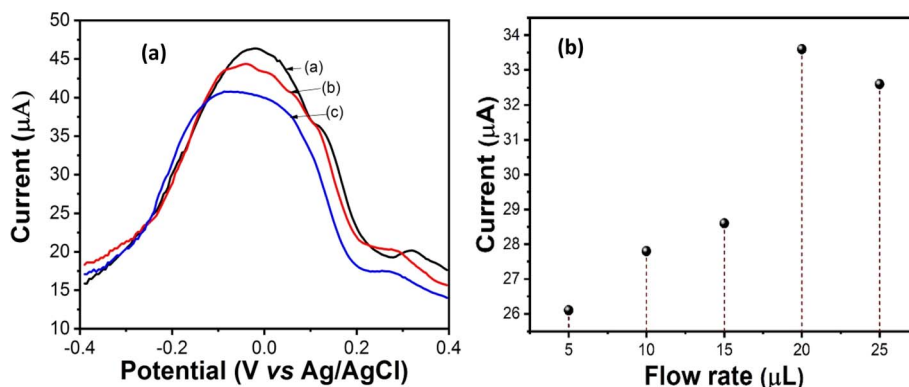
Fig. 5 (a) Differential pulse voltammetry responses of different modified electrodes of (a) nano-ceria/ITO, (b) anti-IL8/nano-ceria/ITO, (c) BSA/anti-IL8/nano-ceria/ITO conducted in PBS (pH 7.4) containing $[Fe(CN)_6]^{3-/4-}$ in the microfluidic system; (b) differential pulse voltammetry responses of nano-ceria/ITO electrode with different flow rates (5 to 25 μL min^{-1}) of PBS (pH 7.4) containing $[Fe(CN)_6]^{3-/4-}$ across the microchannel using a syringe pump.

Moreover, the value of the peak current (44.14 μA) decreased after immobilization of anti-IL8 onto the nano-ceria/ITO substrate inside the microfluidic environment. These results indicate that the electron tunneling distance between anti-IL8 and the electrode surface increased, causing a slower transfer of electrons. When the fabricated electrode surface was treated with BSA it may be noted that the magnitude of the peak current (40.14 μA) decreased, revealing blocking of non-binding sites of anti-IL8 antibodies that hindered the transfer of electrons between the electrode and electrolyte. This study revealed that the presence of BSA on the anti-IL8/nano-ceria/ITO surface blocks non-specific binding sites of IgG that perhaps insulate the electrode and perturb electron communication.

Fig. 5(b) presents flow rate studies of a fabricated microfluidic nano-ceria/ITO electrode with PBS (pH 7.4) containing $[Fe(CN)_6]^{3-/4-}$. The DPV measurement was carried with control over the different flow rates across the microchannels by a syringe pump with a rate of 5 to 25 μL min^{-1}. It was found that current signals increase with an increase in the flow rate from 5 to 20 μL min^{-1}, after which the current value decreases with increasing flow rate. Therefore, the maximum current value was found at a flow rate of 20 μL min^{-1}. Therefore, microfluidic DPV measurements were carried out at a flow rate of 20 μL min^{-1}.

Reynold's number was calculated to determine the behavior of the liquid present in the fabricated microfluidic chip. Reynold's number is a measure of inertial force to viscous force in a liquid medium under capillary action, as depicted in eqn (10):[40]

$$Re = \frac{\rho v L}{\mu} \quad (10)$$

where ρ is the density of the buffer, i.e. the PBS used is 1000 kg m^{-3}, μ is the viscosity of the PBS buffer, which is 0.0008882 Pa s, L is the microfluidic channel length of 0.0025 m and v is the flow rate of the fluid in the microfluidic channel, which is 20 μL min^{-1}. The calculated Re value is found to be 9.9218, confirming the laminar flow of buffer solution in the microchannel inside the microfluidic chip.

3.4 Analytical biosensing performance of the developed immunosensor for IL8 detection

During DPV measurement, a constant potential range from −0.4 to +0.4 V was applied between the working and reference (Ag/AgCl) electrodes, so the corresponding current response was obtained between counter and working electrodes. Here, DPV was used to measure the biosensing signal responses for IL8 biomarker detection. In the process of measurement, 10 μL of each IL8 antigen concentration (0.004 to 10 ng mL^{-1}) were mixed with 2 mL of redox couple electrolyte i.e. PBS containing $[Fe(CN)_6]^{3-/4-}$. These prepared standard solutions from lower to higher concentration were injected into the microfluidic chip inlet using a syringe pump under a controlled flow rate of 20 μL min^{-1}. After that, electrochemical biosensing studies were performed with various IL8 concentrations ranging from 0.004 ng mL^{-1} to 10 ng mL^{-1} in 0.2 M PBS containing 5 mM of $[Fe(CN)_6]^{3-/4-}$. Fig. 6(a) shows the DPV current response of BSA/anti-IL8/nano-ceria/ITO electrodes as a function of IL8 concentration. It is observed that the magnitude of the peak current declined with sequential increments in IL8 concentration. This confirms that the IL8 biomolecule interacts with the BSA/anti-IL8/nano-ceria/ITO surface due to immunocomplex formation between antigen and antibody. The formation of an immunocomplex slows the electron transfer rate between the electrode and electrolyte of the $[Fe(CN)_6]^{3-/4-}$ redox probe, resulting in a decrease in the current signal.

Fig. 6(b) shows the calibration curve plotted using the obtained current values with respect to the various concentrations of IL8. The linear equation achieved from the calibration plot by a linear fit function was $y = -2.75 \times$ log concentration (ng mL^{-1}) + 11.21 with a linear regression coefficient (R^2) of 0.9636. The LOD of the developed immunosensor was 0.0001 ng mL^{-1}, calculated using the standard formula $3\sigma/m$, where σ is the standard deviation and m is the slope. The LOQ was found to be 0.0006 ng mL^{-1}. The improved and significant increase in the electrochemical properties and biosensing characteristics is primarily due to the presence of nano-ceria on the electrode surface. Nano-ceria is a tremendous material owing to its
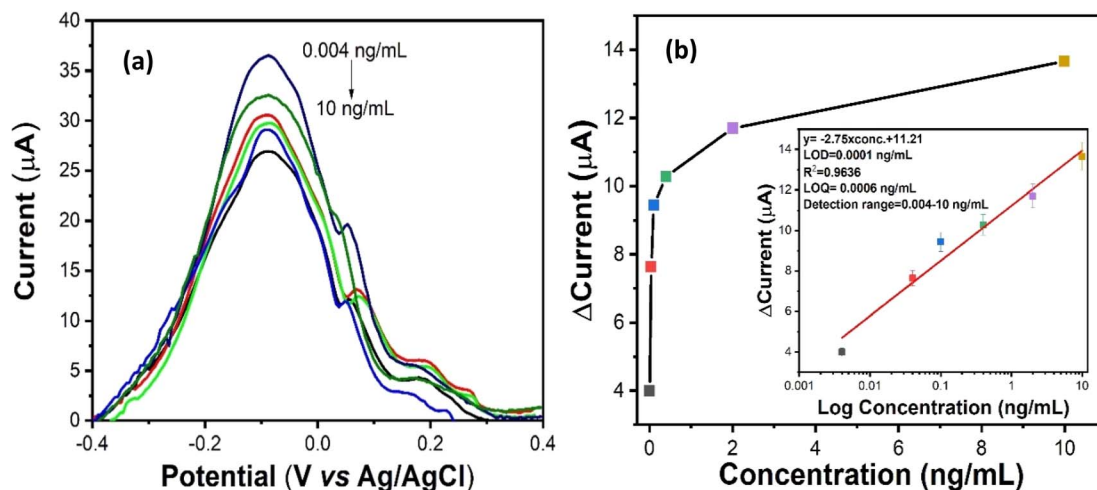
Fig. 6 (a) Differential pulse voltammetry current response signals of the BSA/anti-IL8/nano-ceria/ITO electrode with respect to IL8 biomarker concentration ranging from 0.004 to 10 ng mL^{-1} conducted in 0.2 M PBS containing 5 mM of [Fe(CN)$_6$]$^{3-/4-}$; (b) calibration response curve between change in current value as a function of IL8 concentration ranging from 0.004 to 10 ng mL^{-1} [inset: linear calibration plot of change in current response signal with log function of IL8 concentration from 0.004 to 10 ng mL^{-1}].

unique properties, such as high mechanical strength, oxygen ion conductivity, wide band gap (3.4 eV), biocompatibility and good biological activities. Nano-ceria possesses good electrochemical catalytic properties and acts as a biological antioxidant due to the Ce^{3+}/Ce^{4+} charged moieties on the nano-ceria particles. The integration of nano-ceria onto the electrode surface improves the electrochemical characteristics due to the higher surface area with abundant availability of active sites which can enhance the adsorption of biomolecules. Hence, it improves the overall electrochemical biosensing signals.[43]

Fig. 7 shows the detailed mechanism of nano–bio conjugation onto a microfluidic chip using EDC : NHS chemistry. The presence of the carboxylic functional group (–COOH) of anti-IL8 at the F$_c$ region was activated by EDC : NHS chemistry. The water-soluble nature of EDC acts as a crosslinker and NHS acts as an activator that also increases the stability of the carbodiimide-crosslinked product. When the –COOH

functional group of anti-IL8 gets attached to EDC molecules, an unstable o-acylisourea product is formed. After that, EDC gets detached and the NHS group binds with anti-IL8 by forming more stable esters. When the chemically activated F$_c$ region of anti-IL8 is immobilized onto nano-ceria/ITO substrate, the existing oxygen group of nano-ceria gets bound with the EDC : NHS-activated anti-IL8 to form a metal–ester complex.[40] Also, the presence of a positive charge on nano-ceria materials can also bind with –COOH-activated anti-IL8 through electrostatic interaction.[44] Then, the F$_{ab}$ region for antigen binding sites having free amino terminal groups in the Y-shaped antibody, binds with carboxyl group of IL8 antigen, resulting the formation of an antigen–antibody immunocomplex. In the process of measurement, 10 μL of each IL8 antigen concentration (0.004 to 10 ng mL^{-1}) were mixed with 2 mL of redox couple electrolyte, *i.e.* PBS containing [Fe(CN)$_6$]$^{3-/4-}$. These prepared standard solutions from lower to higher concentration were injected at
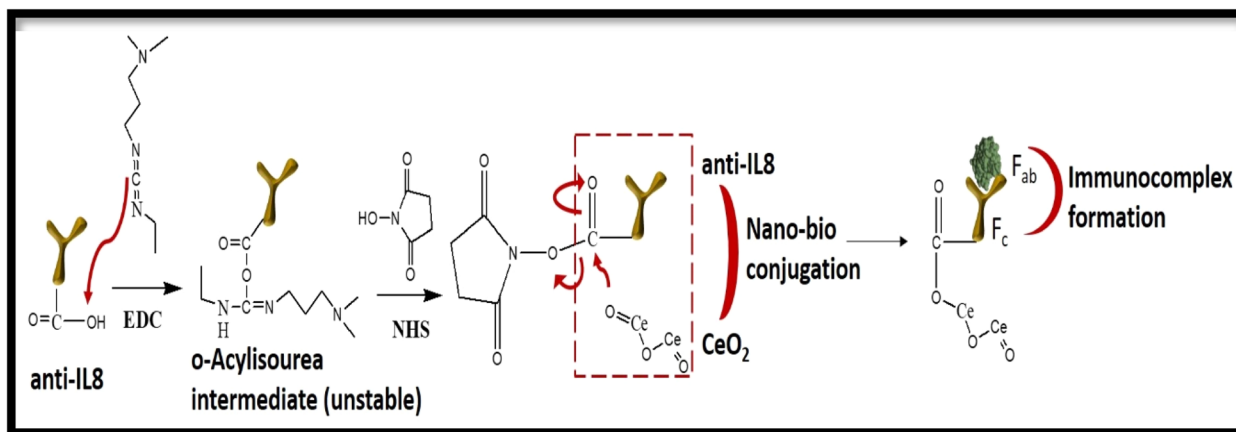

Fig. 7 Mechanism of activation of IL8 antibody using EDC : NHS chemistry, binding with nano-ceria for nano–bio conjugation and attachment of activated antibody with antigen for immunocomplex formation.

regular time intervals into a microfluidic chip containing BSA/anti-IL8/nano-ceria/ITO through an inlet using a syringe pump under a controlled flow rate of 20 μL min^{-1}. With increasing concentration of IL8, the change in the current signal was recorded, as shown in Fig. 6(b), revealing the successful formation of an antigen–antibody immunocomplex.

Several research articles have been published for the detection of IL8 biomarker, but the main challenge remains achieving high sensitivity with a low detection limit, stability, specificity and their practical applicability in clinical samples. This is crucial for the early detection of IL8 in bodily fluids, such as saliva, which is important for reducing morbidity and mortality in cancer patients. For example, Verma *et al.* have developed an electrochemical immunosensor for IL8 biomarker detection using AuNPs–rGO nanomaterial on an ITO electrode.[31] This developed immunosensor worked for a detection range from 0.0005 to 4 ng mL^{-1} with a detection LOD of 0.072 ng mL^{-1}. Similarly, Pachauri *et al.* reported work on the detection of an IL8 biomarker using silver molybdate nanoparticles.[32] This fabricated immunosensor showed a linear detection range from 1×10^{-6} to 40 ng mL^{-1} and LOD of 0.09 ng mL^{-1}. Therefore, this present work is focused on developing a miniaturized electrochemical biosensing platform for oral cancer IL8 biomarker detection with good biosensor performance in terms of high sensitivity, selectivity, specificity, and wide detection range with low limits of detection and quantification along with their practical use in clinical human saliva samples. The excellent biosensing performance of the constructed biosensor makes it useful for the detection of other cancer biomarkers using their respective bio-recognition elements. To the best of our knowledge, this is the first report on a microfluidic-based electrochemical immunosensor for the detection of IL8 biomarker. In this current study, the presence of nano-ceria over the ITO electrode in a microfluidic chip provides significant signal enhancement like in terms of current. This may be attributed to the excellent Ce^{3+}/Ce^{4+} charge moieties on the nano-ceria particles with good electrochemical catalytic properties, high mechanical strength, high permeability, biocompatibility, large active surface area, and better electron transportation between electrode and electrolyte. Therefore, nano-ceria is a promising candidate for the development of an electrochemical biosensor for IL8 biomarker detection. Moreover, Table 1 shows a comparison of the analytical parameters from previously reported research articles with the present work for cancer biomarker detection. Noticeably, important biosensing characteristics have been enhanced using the nano-ceria based IL8 detection.

3.5 Repeatability and interference study with various interferents

Repeatability studies of the fabricated nano–biochip were carried out using five similarly prepared BSA/anti-IL8/nano-ceria/ITO electrodes under similar experimental conditions with IL8 biomarker concentration of 10 ng mL^{-1} [Fig. 8(a)]. All the fabricated nano–biochips show almost the same current response with the concentration of antigen and the coefficient of variation was found to be 0.028 and the relative standard deviation (RSD) was 3.16. These results indicate that developed biosensor achieved precise and reproducible detection of IL8.

Also, selectivity and specificity studies of the fabricated microfluidic nano–biochip of BSA/anti-IL8/nano-ceria/ITO were performed for the IL8 cancer biomarker. Some interfering analytes were selected for interference studies with IL8 cancer biomarker, including NaCl, glucose, Cyfra-21, TNF-α, CA-125, and CEA. To carry out interference studies, 10 μL of each interferent was added to electrolyte solution and corresponding current response was recorded using DPV. Fig. 8(b), shows the response of the current using a BSA/anti-IL8/nano-ceria/ITO nano–biochip for the IL8 biomarker in the presence of other interferents. It is observed that the magnitude of the current did not display a variation in the presence of other interfering species in comparison to the current response of the IL8 biomarker. Also, the RSD was calculated using the IL8 response with respect to other interferents, such as NaCl, glucose, Cyfra 21, TNF-α, CA-125, and CEA. The RSD value found to be in the range of 0.78 to 3.21. This insignificant variation in the current response signal suggests that the BSA/anti-IL8/nano-ceria/ITO nano–biochip is highly specific towards the IL8 biomarker.

3.6 Real sample studies

In order to validate the performance of the fabricated microfluidic nano–biochip for IL8 detection, studies of real spiked samples were carried out using saliva samples. In this study, various concentrations of saliva samples were prepared by spiking with known concentrations of IL8 biomarker. Details of

Table 1 Comparison of analytical parameters of published research work related to IL8 biosensors with the results of the present work[a]

S. no.	Matrix	Technique	Detection range (ng mL^{-1})	Limit of detection (ng mL^{-1})	Ref.
1	Anti-IL8 IgG1/CM5 sensor chip	SPR	0.0095–0.191	0.0025	45
2	Anti-IL8/AuNPs–rGO/ITO	DPV	0.0005–4	0.072	31
3	BSA/anti-IL8/β-Ag$_2$MoO$_4$/ITO	DPV	1×10^{-6}–40	0.09	32
4	Aminothiol/activated MWCNT/anti-IL8	EIS	0.001–1.0	0.0001	1
5	Anti-IL8/aptamer/APTES	Fluorescence	0.0075–0.12	0.00084	46
6	BSA/anti-IL8/nano-ceria/ITO	DPV	0.004–10	0.0001	Present work

[a] CM: carboxymethyl dextran, AuNPs: gold nanoparticles, rGO: reduced graphene oxide, BSA: bovine serum albumin, MWCNT: multiwalled carbon nanotube, APTES: (3-aminopropyl)triethoxysilane, SPR: surface plasmon resonance, DPV: differential pulse voltammetry, EIS: electrochemical impedance spectroscopy.
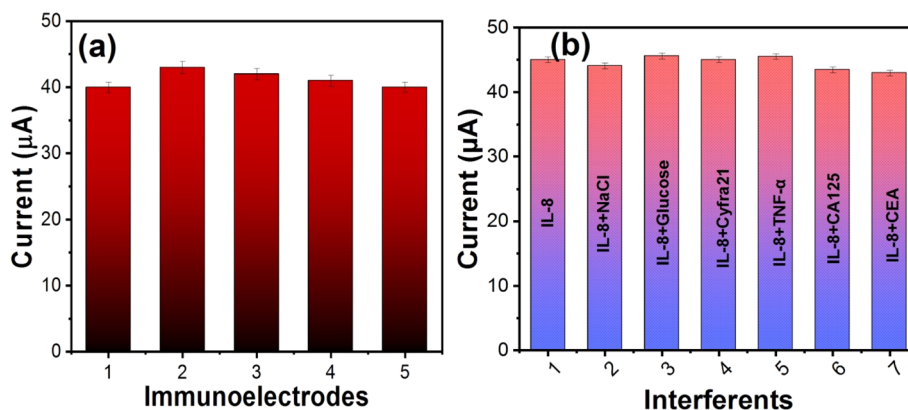
Fig. 8 (a) Repeatability study of five different nano–biochips of BSA/anti-IL8/nano-ceria/ITO; (b) interference study of fabricated BSA/anti-IL8/nano-ceria/ITO electrode with antigen of IL8 and other interferents using the DPV technique.

Table 2 The results of real spiked samples of IL8 in saliva using the fabricated BSA/anti-IL8/nano-ceria/ITO nano–biochip

S. no.	Sample taken	Spiked concentration (ng mL^{-1})	Found concentration (ng mL^{-1})	RSD	% recovery
1	Saliva sample	0.1	0.09	2.96	95.8
2		0.4	0.39	0.958	98.65
3		2.0	2.02	0.812	101.1

this experiment are described in Experimental section 2.6. Table 2 shows the analytical results of spiked IL8 concentrations (0.1, 0.4 and 2.0 ng mL^{-1}) and the RSD values were found to be 2.96, 0.958 and 0.812, respectively. Also, the percentage recovery was calculated with concentrations of IL8 of 0.1, 0.4 and 2.0 ng mL^{-1} and found to be in the range of 95–101.1%. Hence, the results obtained from this study of spiked samples revealed that the developed microfluidic IL8 biosensor has the capability to detect IL8 in saliva samples.

4. Conclusions

The face centered lattice cubic fluorite structure of nano-ceria particles were prepared with a simple co-precipitation preparation method. The optical, structural and surface morphology of the nano-ceria was investigated through various techniques including UV-visible spectrocopy, XRD, FT-IR, Raman spectroscopy, TEM, SEM, and EDX analysis. Nano-ceria particles of spherical shape with an average diameter of 8.13 nm were prepared. Elemental mapping and EDX confirmed the existence of cerium and oxygen elements in the nano-ceria. The presence of functional groups and bonding with antibodies were confirmed by FT-IR spectroscopy, demonstrating the successful immobilization of anti-IL8 antibodies onto the nano-ceria electrode surface. For the development of a microfluidic nano–biochip, three electrode patterns of working, reference and counter electrodes on a microfluidic chip (3 × 4 cm) were prepared using a maskless photolithography technique and molding of a PDMS elastomer with a 200 μm wide and 2 cm long microchannel. For electrochemical biosensing response studies, DPV was used and a linear response was found with

increasing concentration of IL8 antigen. This developed microfluidic IL8 biosensor worked linearly in the concentration range from 0.004 to 10 ng mL^{-1}, with LOD and LOQ of 0.0001 ng mL^{-1} and 0.0006 ng mL^{-1}, respectively. For validation of the nano–biochip, a study of spiked saliva samples was carried out with the fabricated nano–biochip, showing favorable electrochemical responses and a high percentage of recovery rate (95–101.1%). Also, a fabricated microfluidic nano–biochip of BSA/anti-IL8/nano-ceria/ITO is selective towards IL8 analyte and showed good repeatability results. This fabricated nano–biochip of BSA/anti-IL8/nano-ceria/ITO platform may hold promise for detecting other biomarkers by modifying the surface using their respective bio-recognition elements, providing a versatile platform for POC diagnostics.

Data availability

Data will be available on request.

Conflicts of interest

The authors declare that they have no conflict of interest.

Acknowledgements

References

1 S. Azzouzi, M. Ben Ali, F. Bellagambi, A. Elaissari, N. Jaffrezic-Renault, A. Errachid and N. Zine, *Talanta*, 2022, **246**, 123436.

2 P. Kuppusamy, N. Govindan, M. M. Yusoff and S. J. A. Ichwan, *Saudi J. Biol. Sci.*, 2017, **24**, 1212–1221.

3 R. Gasparri, G. Sedda and L. Spaggiari, *J. Clin. Med.*, 2020, **9**, 1790.

4 U. Landegren and M. Hammond, *Mol. Oncol.*, 2021, **15**, 1715–1726.

5 N. C. Japp, J. J. Souchek, A. R. Sasson, M. A. Hollingsworth, S. K. Batra and W. M. Junker, *J. Immunol. Res.*, 2021, **2021**(1), 9942605.

6 E. Dama, T. Colangelo, E. Fina, M. Cremonesi, M. Kallikourdis, G. Veronesi and F. Bianchi, *Cancers*, 2021, **13**, 3919.

7 N. J. Vickers, *Curr. Biol.*, 2017, **27**, R713–R715.

8 R. Bhawal, A. L. Oberg, S. Zhang and M. Kohli, *Cancers*, 2020, **12**, 2428.

9 S. Sornambikai, H. Amir, G. Bhuvaneshwari, N. Ponpandian and C. Viswanathan, *ECS Sens. Plus*, 2022, **1**, 21602.

10 D. Vozgirdaite, H. Ben Halima, F. G. Bellagambi, A. Alcacer, F. Palacio, N. Jaffrezic-Renault, N. Zine, J. Bausells, A. Elaissari and A. Errachid, *Chemosensors*, 2021, **9**, 26.

11 H. Ben Halima, F. G. Bellagambi, A. Alcacer, N. Pfeiffer, A. Heuberger, M. Hangouët, N. Zine, J. Bausells, A. Elaissari and A. Errachid, *Anal. Chim. Acta*, 2021, **1161**, 338468.

12 P. R. Sreelakshmi, S. Nair, B. Soman, R. Alex, K. Vijayakumar and V. R. Kutty, *J. Fam. Med. Prim. Care*, 2015, **4**, 395.

13 A. S. Gokhale, R. I. Haddad, L. A. Cavacini, L. Wirth, L. Weeks, M. Hallar, J. Faucher and M. R. Posner, *Oral Oncol.*, 2005, **41**, 70–76.

14 J. A. Stenken and A. J. Poschenrieder, *Anal. Chim. Acta*, 2015, **853**, 95–115.

15 T. P. Kobawala, G. H. Patel, D. R. Gajjar, K. N. Patel, P. B. Thakor, U. B. Parekh, K. M. Patel, S. N. Shukla and P. M. Shah, *J. Thyroid Res.*, 2011, **2011**(1), 270149.

16 V. Merz, C. Zecchetto, R. Santoro, F. Simionato, F. Sabbadini, D. Mangiameli, G. Piro, A. Cavaliere, M. Deiana and M. T. Valenti, *Clin. Cancer Res.*, 2020, **26**, 4661–4669.

17 S. Shekhar, A. K. Yadav, A. Khosla and P. R. Solanki, *ECS Sens. Plus*, 2022, **1**, 41601.

18 M. W. Lingen, E. Abt, N. Agrawal, A. K. Chaturvedi, E. Cohen, G. D'Souza, J. Gurenlian, J. R. Kalmar, A. R. Kerr and P. M. Lambert, *J. Am. Dent. Assoc.*, 2017, **148**, 712–727.

19 M. M. A. Chiamulera, C. B. Zancan, A. P. Remor, M. F. Cordeiro, F. O. Gleber-Netto and A. R. Baptistella, *BMC Cancer*, 2021, **21**, 205.

20 F. Elmahgoub, *Evid.-Based Dent.*, 2022, **23**, 30–31.

21 K. R. Khondakar, M. A. Kachouei, F. E. Erukainure and M. A. Ali, *ECS Sens. Plus*, 2023, **2**, 43403.

22 R. Fan, Y. Li, K.-W. Park, J. Du, L. H. Chang, E. R. Strieter and T. L. Andrew, *ECS Sens. Plus*, 2022, **1**, 10601.

23 C. Cheng, H. Wang, J. Zhao, Y. Wang, G. Zhao, Y. Zhang, X. Liu and Y. Wang, *Colloids Surf., B*, 2024, 113767.

24 P. C. Gomes-Junior, G. P. Longatto, K. K. d. L. Augusto, J. d. S. Rocha, E. Piccin and O. Fatibello-Filho, *Microchim. Acta*, 2024, **191**, 425.

25 T. K. Dhiman, G. Lakshmi, A. Roychoudhury, S. K. Jha and P. R. Solanki, *ChemistrySelect*, 2019, **4**, 4867–4873.

26 S. Radhakrishnan, M. Mathew and C. S. Rout, *Mater. Adv.*, 2022, **3**, 1874–1904.

27 F. Haghayegh, R. Salahandish, A. Zare, M. Khalghollah and A. Sanati-Nezhad, *Lab Chip*, 2022, **22**, 108–120.

28 J. Ozhikandathil, S. Badilescu and M. Packirisamy, *ECS Sens. Plus*, 2022, **1**, 23201.

29 K. Awawdeh, M. A. Buttkewitz, J. Bahnemann and E. Segal, *Microsyst. Nanoeng.*, 2024, **10**, 100.

30 V. Kamat, L. Burton, V. Venkadesh, K. Jayachandran and S. Bhansali, *ECS Sens. Plus*, 2023, **2**, 43201.

31 S. Verma, A. Singh, A. Shukla, J. Kaswan, K. Arora, J. Ramirez-Vick, P. Singh and S. P. Singh, *ACS Appl. Mater. Interfaces*, 2017, **9**, 27462–27474.

32 N. Pachauri, G. B. V. S. Lakshmi, S. Sri, P. K. Gupta and P. R. Solanki, *Mater. Sci. Eng., C*, 2020, **113**, 110911.

33 Y. Wu, C. Wang, P. Wang, C. Wang, Y. Zhang and L. Han, *RSC Adv.*, 2021, **11**, 8124–8133.

34 H.-Y. Lei, Z.-Z. Wang, Y.-C. Chen, C.-S. Kuo, C.-H. Yang and C.-H. Huang, in *Microfluidics, BioMEMS, and Medical Microsystems XVIII*, SPIE, 2020, vol. 11235, pp. 19–25.

35 F. Charbgoo, M. Ramezani and M. Darroudi, *Biosens. Bioelectron.*, 2017, **96**, 33–43.

36 M. A. Ali, P. R. Solanki, M. K. Patel, H. Dhayani, V. V. Agrawal, R. John and B. D. Malhotra, *Nanoscale*, 2013, **5**, 2883–2891.

37 H. Bhardwaj, C. A. Marquette, P. Dutta, Rajesh and G. Sumana, *Anal. Bioanal. Chem.*, 2020, **412**, 7029–7041.

38 H. Bhardwaj, M. K. Pandey, Rajesh and G. Sumana, *Microchim. Acta*, 2019, **186**, 1–12.

39 N. Pachauri, K. Dave, A. Dinda and P. R. Solanki, *J. Mater. Chem. B*, 2018, **6**, 3000–3012.

40 A. K. Singh, T. K. Dhiman, G. Lakshmi, R. Raj, S. K. Jha and P. R. Solanki, *Nanotechnology*, 2022, **33**, 285501.

41 H. Bhardwaj, G. Sumana and C. A. Marquette, *Talanta*, 2021, **222**, 121578.

42 H. Bhardwaj, C. Singh, M. k. Pandey and G. Sumana, *Sens. Actuators, B*, 2016, **231**, 624–633.

43 S. Rajeshkumar and P. Naik, *Biotechnol. Rep.*, 2018, **17**, 1–5.

44 Y. W. Hartati, L. K. Letelay, S. Gaffar, S. Wyantuti and H. H. Bahti, *Sens. Bio-Sens. Res.*, 2020, **27**, 100316.

45 C.-Y. Yang, E. Brooks, Y. Li, P. Denny, C.-M. Ho, F. Qi, W. Shi, L. Wolinsky, B. Wu and D. T. W. Wong, *Lab Chip*, 2005, **5**, 1017–1023.

46 J. Verbarg, O. Hadass, P. D. Olivo and A. Danielli, *Sens. Actuators, B*, 2017, **241**, 614–618.